



Derivation of both EDLC and pseudocapacitance characteristics based on synergistic mixture of NiCo_2O_4 and hollow carbon nanofiber: An efficient electrode towards high energy density supercapacitor

Gracita M. Tomboc, Hern Kim*

Department of Energy Science and Technology, Smart Living Innovation Technology Center, Myongji University, Yongin, Gyeonggi-do, 17058, Republic of Korea

ARTICLE INFO

Article history:

Received 9 April 2019

Received in revised form

3 June 2019

Accepted 18 June 2019

Available online 19 June 2019

Keywords:

Carbon nanofiber

NiCo_2O_4

Dual nozzle electrospinning

Hydrothermal treatment

ABSTRACT

In this study we fabricated a hollow carbon nanofiber (CNF) via a facile dual nozzle electrospinning process and directly used as low-cost and environmental friendly carbon source material, which were incorporated to NiCo_2O_4 (NCO). We designed a hybrid nanocomposite based on synergistic mixture of hollow structure CNF and spinel NCO, with 3D dandelion like morphology, hierarchical mesoporous surface, high specific surface area, and directly grown onto the surface of nickel foam substrate. We modified the structural properties of hybrid NCO–CNF nanocomposite in aim to improve its overall electrochemical performance towards supercapacitor application. In here, we fabricated our hollow CNF using dual concentric nozzle electrospinning method, comprising of poly (vinyl pyrrolidone) (PVP) as soluble core and polyacrylonitrile (PAN) as shell. It was essential in our study to fully leach out the PVP to obtain a hollow structure: this hollow structure of CNF provided a conductive network that guaranteed the high speed movement of electron/electrolyte. Furthermore, the overall specific capacitance and energy density of the hybrid NCO–CNF electrode were remarkably boost up due to the derivation of both electric double layer capacitance and pseudocapacitance characteristics based on the synergistic mixture of graphitic carbon and transition metal oxides. The fabricated binder-free hybrid NCO–CNF electrode displayed efficient charge transfer and achieved outstanding specific capacitance and energy density as high as 1188.19 F g^{-1} and $37.23 \text{ W h kg}^{-1}$, respectively, even at high current density of 50 A g^{-1} .

© 2019 Published by Elsevier Ltd.

1. Introduction

For the past years, supercapacitors (SCs) has been acknowledged as one of the most promising energy storage device owing to its multiple great characteristics such as high power density, long cycle lifespan, and fast charge/discharge rates [1–3]. However, up to this date, researchers devoted to SCs work are still looking for stable and feasible solution that may effectively boost up the energy density of such energy storage device [4]. There has been many proposed ways on how to tackle such problem, and most current is to either increase the overall specific capacitance or to widen the operating potential window; both proposals have its own advantages and limitations [5,6]. For instance, one who wants to increase the specific capacitance of the SCs may focus on

structural modifications of present electrode materials. At this point, electrode materials can be categorized into three main groups: (1) carbon materials [7], (2) conductive polymers [8], and (3) transition metal oxide (TMO) [9]; all of which were reported of having great potential to be an effective electrode for supercapacitor, but all have their own downside that limits them to be used for practical applications. For example, carbon materials such as carbon nanotubes (CNT), activated carbon, graphitic carbon, and carbon nanofiber (CNF), exhibit inferior specific capacitance and limited energy density [10,11], while conductive polymers such as polyaniline and polypyrrole suffer from poor electrical stability [12,13], and TMO such as cobalt-based metal oxides (NiCo_2O_4 , ZnCo_2O_4 , MnCo_2O_4 , CuCo_2O_4 , etc) display low rate capability and weak cycling stability [14–17]. Due to these disadvantages, a further study about structural modifications on these potentially excellent materials are still very much needed.

Among the present carbon materials, CNT has always been referred to as most efficient due to its outstanding electrical

* Corresponding author.

E-mail address: hernkim@mju.ac.kr (H. Kim).

conductivity, excellent mechanical and chemical properties, and impressive surface area [18–20]. However, the fabrication method of this material requires high amount of energy and highly concentrated acid in big volume that is truly harmful to our environment. On the other hand, CNF is a promising carbon source material not only because of its great chemical stability and flexibility but as well as because of its enhance electron conductive pathway due to its continuous interconnected porous structure [21–23]. However, CNF suffer from low specific capacitance because of its low surface area [24]; thus a fabrication method to increase the surface area of CNF is needed. Numerous methods have been used to fabricate CNF, including the catalytic chemical vapor deposition (CVD) growth, template based synthesis, biomass methods and electrospinning; compared to other methods, electrospinning shows the advantages of flexibility, simplicity, high efficiency and production rate [25]. Moreover, hollow CNF represent a new generation of CNF structures with double the surface area. Compared with traditional electrospun nanofibers, hollow structure CNF provides extra inner surfaces and that the micro-mesopores can effectively increase the specific surface area and pore volume, which is very beneficial for enhancing its electrochemical performance. Previous studies that fabricated CNF via electrospinning method had reported to used 2 or more combination of polymer solutions with different additives to improve the overall performance of the nanofiber, and then submitted into multi-steps heat treatment at high temperatures for long time to achieve the desired hollow structures [26–28]. In here, we intentionally increased the specific surface area of simple CNF by designing a hollow structure via a facile dual electrospinning process containing of soluble core and flexible shell. The hollow structure of the CNF was simply obtain through leaching out process using dilute water. Overall, the method and raw materials that we have used are cost-efficient and sustainable; it is simple and straightforward that can be potentially use for large scale production. Furthermore, NiCo_2O_4 has been acknowledged as one of the most efficient and superior pseudocapacitive material towards energy storage applications due to its outstanding characteristics such as high theoretical capacity and richer redox reaction benefited from both Ni and Co cations [29–31]. Unfortunately, up to date, single NiCo_2O_4 still suffers from poor rate capability and inferior cycling stability because of low electrical conductivity and small surface area [32].

In this study, we designed a hybrid nanocomposite electrode containing a synergistic mixture of hollow CNF and spinel NiCo_2O_4 ; it's highly strategic to utilize the excellent electrochemical properties of both materials and to complement their specific limitations by incorporating them together to make one great final material. The hollow structure of fabricated CNF is expected to provide a highway for faster and easier electron/electrolyte movement, and that its superior electronic conductivity is intended in improving the rate capability and cycling stability of the nanocomposite even at high current density. Additionally, the numerous electroactive sites provided by spinel NiCo_2O_4 is anticipated to enhance the specific capacitance and energy density of the nanocomposite. Finally, we used the metal salts seeding method to directly grow these nanocomposite onto the surface of nickel foam substrate to fabricate a binder-free electrode and then further used as an ideal electrode towards supercapacitor application. Overall, the electric double layer capacitance (EDLC) and pseudocapacitance arising from both of the CNF and NiCo_2O_4 , respectively, were added up together which effectively boost up the total specific capacitance of this hybrid electrode that lead to exceptional energy density and excellent cycling stability even at high current density.

2. Materials and methods

2.1. Materials

All materials were used as received. Polyacrylonitrile (PAN, MW: 150 000) and Urea ($\text{CO}(\text{NH}_2)_2$, 99–100.5%) were purchased from Sigma Aldrich. N,N-Dimethylformamide (DMF, 99%) and Nickel (II) nitrate hexahydrate ($\text{N}_2\text{NiO}_6 \cdot 6\text{H}_2\text{O}$) were secured from Alfa Aesar. Polyvinylpyrrolidone (PVP, MW: 1 300 000) and Cobalt (II) nitrate hexahydrate ($\text{Co}(\text{NO}_3)_2 \cdot 6\text{H}_2\text{O}$) were purchased from Acros organics. Lastly, Ammonium fluoride (NH_4F) was from Showa Chemical Co. Ltd.

2.2. Dual nozzle electrospinning of PVP-PAN nanofibers

In a typical experiment, PVP and PAN polymer solutions were prepared by dissolving 1.5 g PVP and 0.8 g PAN into 10 mL DMF, respectively. The mixture was put in an oil bath set up to maintain the 70 °C temperature and continuously stirred for ~4 h or until homogeneous polymer solution with good viscosity was obtained. The prepared solutions were then used as soluble core (PVP) and shell (PAN) in the dual nozzle electrospinning to obtain the desired hollow structure of PAN nanofibers. The two solutions were loaded into 10 mL disposable syringes, respectively, and were placed in a typical electrospinning set-up; composing of two pumps, a direct current-power supply attached on a dual concentric nozzle (NNC-DN 17G – 23G) and metal collector covered up with aluminum foil. Finally, the feeding rate of the solutions were maintained at 0.9 mL h⁻¹ (core) and 0.018 mL h⁻¹ (shell) with applied voltage of 17 kV.

2.3. Fabrication of hollow carbon nanofiber (CNF)

The collected PVP-PAN nanofiber mat was soaked in 400 mL dilute water to leach out the PVP and leave the core hollow. PVP is very soluble with water so that ideally, the moment it touch the water it will be easily leached out from the core of the nanofiber, leaving the PAN shell with some pores on its surface. After 4–6 h of soaking the nanofiber into dilute water, it was removed and dried in drying oven at 75 °C for 24 h to remove moisture content. The dried nanofiber, with assumed hollow structure, was then submitted into two-steps carbonization process: (1) pre-oxidation at 250 °C for 1 h with heating rate of 5 °C h⁻¹ under air atmosphere, and (2) carbonization at 800 °C for 2 h with heating rate of 3 °C h⁻¹ under nitrogen atmosphere. Afterwards, the texture of the final CNF became too hard but fragile or became too brittle. Thus, the as-prepared hollow CNF was carefully grinded until powder form and then directly used as carbon-based material for the synthesis of the desired hybrid nanocomposite.

2.4. Synthesis of the hybrid nanocomposite composing of hollow CNF and spinel NiCo_2O_4

Metal salts solution was prepared by dissolving a mixture of 2.91 g $\text{N}_2\text{NiO}_6 \cdot 6\text{H}_2\text{O}$, 5.82 g $\text{Co}(\text{NO}_3)_2 \cdot 6\text{H}_2\text{O}$, 0.74 g NH_4F , and 3.6 g $\text{CO}(\text{NH}_2)_2$ in 40 mL de-ionized (DI) water by continuous stirring for 1 h at room temperature. Simultaneously, the as-prepared CNF was carefully grinded using mortar and pestle, and 0.025 g of which was dispersed in 40 mL DI water under ultrasonication for 1.5 h. Furthermore, the two solutions were mixed and continued stirring for another hour or until they form a homogenous solution. Then it was transferred in 250 mL transparent borrosil bottle where 2 × 1 cm cleaned nickel foam (NF) was placed standing on the wall. The metal salts-CNf solution was submitted in facile hydrothermal treatment for 12 h at 120 °C. Afterwards, the fully coated NF was

collected, submerged in small amount of DI water and put under ultrasonication for 5 min to remove any excess growth (layer) of NiCo–CNF precursor. It was further washed with DI water and ethanol multiple times before putting in drying oven at 75 °C for 24 h. Finally, the NF coated with NiCo–CNF composite was annealed at 450 °C for 3 h with heating rate of 3 °C h⁻¹ under air atmosphere.

2.5. Characterization

Thermogravimetric and differential thermal analysis (TGA-DTA; TGA-N100 instrument, 30–800 °C with 10 °C min⁻¹ heating rate under air atmosphere) were performed to determine the degradation temperature and thermal behaviour of the following samples: (a) PVP nanofiber (nf), (b) PAN nf, (c) PVP-PAN nf (fresh), (d) PAN nf (after leaching out PVP core). Furthermore, FTIR (Nicolet iS5 model, 4000 to 500 cm⁻¹ wavelength), Raman spectroscopy (Raman microscope 8228, Renishaw), XRD (Cu–K radiation = 1.540 Å, 10–90° bragg angle), and XPS (Thermo Electron, U.K, Mg Ka radiation) were utilized to confirm the functional groups, graphitization order, crystal structure, and chemical state, respectively, of fabricated CNF and synthesized NCO–CNF nanocomposite. Moreover, field emission-scanning electron micrography (FESEM; equipped with EDX, Hitachi S–3500N) and high resolution-transmission electron microscopy (HRTEM; JEM-2100F microscope) were used to show the structural morphology of prepared samples. Lastly, physical characterization such as specific surface area, pore volume and pore size diameter were determined by BET method and N₂ adsorption-desorption isotherm.

2.6. Electrochemical measurements

All electrochemical measurements were done using a commercialized ZIVE MP1 multi-channel workstation potentiostat with three-electrode system in 2M KOH aqueous electrolyte. NCO–CNF directly grown on nickel foam substrate (1 × 1 cm) (NCO–CNF @ NF), with calculated mass loading of approximately 1.5 mg was used as working electrode, while Ag/AgCl at 1M KCl and platinum wire were used as reference and counter electrode, respectively.

Before recording any official results, the system was stabilized by running 250 cycles of cyclic voltammetry (CV) test using 50 mV s⁻¹ scan rate and –0.1–0.6 V potential window. CV and galvanostatic charge-discharge (GCD) tests were performed to calculate the specific capacitance of the NCO–CNF @ NF electrode. All CV tests were done within potential window of –0.1–0.6 V and performed at increasing scan rates from 2 to 30 mV s⁻¹, while GCD test were done within potential window of 0–0.475 V at increasing current density from 5 to 50 A g⁻¹. Additionally, energy density were calculated based on the GCD curves. The following equations were used to calculate the specific capacitances and energy density [33–35]:

1. Based on CV curves, $C = \frac{\int i dv}{2 * m * \mu * \Delta V}$
2. Based on GCD curves, $C_s = \frac{I \Delta t}{m * \Delta V}$
3. Energy density, $E = \frac{C_s \Delta V^2}{7.2}$

where C (F g⁻¹) is specific capacitance, i (A) and v (V) are the current and potential, μ (mV s⁻¹) is the scan rate, m (g) is the mass loading of electrode, ΔV (V) is the potential window of discharge, I (A) is discharge current, Δt (s) is discharge time, and E (W h kg⁻¹) is energy density.

Moreover, electrochemical impedance spectroscopy (EIS) measurements were performed within the frequency range of

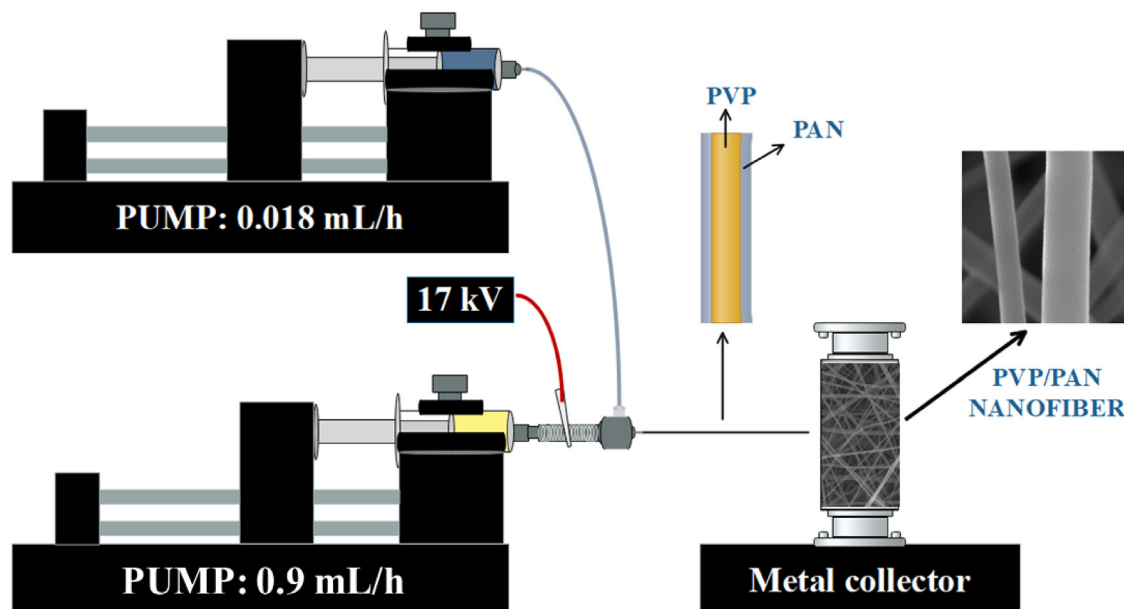
0.1–10 000 Hz with constant bias potential 0.6 V and amplitude of 10 mV. Lastly, stability of the NCO–CNF @ NF electrode was assessed by performing 3000 repeated GCD tests at current density of 30 A g⁻¹ and within 0.0–0.475 V potential window.

3. Results and discussion

3.1. Characterization of hollow CNF

In this study, we tried to fabricate a hollow CNF via a simple dual nozzle electrospinning method; wherein PVP polymer was used as soluble core and PAN polymer as shell. [Schematic diagram 1](#) shows the dual nozzle electrospinning set up that we used. It was vital in our experiment to leach out the PVP from the core of the electrospun PVP/PAN nanofiber for us to obtain the hollow structure. To determine the structure of the electrospun nanofiber, we submitted the following nanofibers to thermogravimetric and differential thermal analysis (TGA-DTA) for thermal behaviour investigation: (a) PVP, (b) PAN, (c) fresh PVP/PAN, and (d) washed PVP/PAN. [Fig. 1\(a\)](#) to [Fig. 1\(d\)](#) show the TGA (black line) and DTA (blue line) profiles for the mentioned nanofibers, respectively. Based on the TGA-DTA profiles of PVP and PAN nanofibers ([Fig. 1\(a\)](#) and [\(b\)](#)), it showed that the major degradation point of the PVP nanofiber is at temperature ~420 °C, while PAN nanofiber degraded at ~300 °C; these results are well parallel to the previous reports [36,37]. These temperatures were used as basis in checking the structure of the electrospun PVP/PAN nanofiber without the visual images. To confirm the removal of PVP from the core of the nanofiber, we compare the TGA-DTA profiles of the fresh PVP/PAN nanofiber from the washed one. [Fig. 1\(c\)](#) is very important as it confirms the presence of the two nanofibers; the detected intense peaks at ~300 °C and 420 °C are strong indication of the existence of both PAN and PVP on the electrospun nanofiber. More importantly, [Fig. 1\(d\)](#) shows the TGA-DTA profile of the washed nanofiber, wherein the peak at 420 °C disappeared after soaking the nanofiber into dilute water for certain time, which confirmed the success removal of PVP core.

To further investigate the structure of the electrospun nanofiber, we performed FESEM and HRTEM for structural analysis. [Fig. 2\(a\)](#) and [\(b\)](#) show the low and high magnification FESEM images of the fresh nanofibers while [Fig. 2\(c\)](#) and [\(d\)](#) are for the washed nanofiber, respectively. The low magnification images of the nanofibers showcase long and continuous fibrous morphologies of the fabricated nanofiber. Additionally, it can be observed on the high magnification images that the surface of the fresh nanofibers is smooth ([Fig. 2\(b\)](#)), but after soaking it into dilute water for couple of hours to leach out the PVP from the core, the surface of the nanofiber became rough and porous ([Fig. 2\(d\)](#)). The roughness and nanopores on the surface of the washed nanofiber may be interpreted as escape holes created by the PVP during the leaching process. Moreover, using high magnification of HRTEM images, we further showcase the structural morphology of the fabricated nanofiber. [Fig. 2\(e\)](#), present clearly the success formation of core-shell structure of PVP/PAN nanofibers, wherein it can be clearly observe the presence of two different nanofibers which is well attributed to PAN and PVP fiber. [Fig. 2\(f\)](#) display the success removal of PVP fiber from the core of the nanofiber, wherein it can be clearly seen that the core of the nanofiber was left hollow. Hollow structure CNF provides extra inner surfaces and that the micro-mesopores on its surface can effectively increase the specific surface area and pore volume, which is very beneficial for enhancing its electrochemical performance [38]. Moreover, [Fig. 3\(a\)–\(d\)](#), are the low and high magnification HRTEM images of the carbonized nanofiber. The sample material was grinded, sonicated and dispersed in ethanol solvent to obtain individual fibers



Scheme 1. Dual nozzle electrospinning set-up.

with nanometer size that will fit for the HRTEM machine. Based from the figures, though at its grinded form, the sample material still obtained its fibrous morphology with open ends, which further illustrate the hollow structure of the CNF. Unfortunately, during our TEM analysis, there were no 3D fiber captured that can show the inner of the fiber; thus these pictures were the clearest that we can obtained.

Additionally, the graphitic structure of the carbon nanofibers was confirmed via Raman spectroscopy. Typical Raman spectra of CNF is shown on Fig. S1(a), with two intense peaks at 1345 cm^{-1} and 1585 cm^{-1} which represent the D- and G-characteristics band. By definition, D-band [39] is the indicator of defects (disordered) on the surface of CNF while G-band [40] characterize the graphitic carbon. The I_D/I_G ratio is computed as 0.85, which indicates the presence of defects introduced on CNF during the carbonization process [41]. Furthermore, FTIR was performed to examine the functional groups present on the prepared PAN-based carbon nanofiber. Fig. S1(b) shows the IR-spectra of carbonized PAN nanofiber [42]; the adsorption peak at 2345 cm^{-1} is assigned to the $\text{C}\equiv\text{N}$ stretching vibration of acrylonitrile unit in the polymer chain. Moreover, adsorption peak at 1378 cm^{-1} (stretching vibration in CH) and 2922 cm^{-1} (stretching vibration in CH_2) are characteristics of aliphatic methylene groups along the PAN backbone. Lastly, adsorption peak at 1610 cm^{-1} is attributed to $\text{C}=\text{C}$ functional groups.

3.2. Characterization of NCO–CNF hybrid nanocomposite

Moreover, we compared the XRD patterns of CNF and the synthesized hybrid NiCo_2O_4 –CNF (NCO–CNF) nanocomposite; both samples were analysed in powder form for better verification of phase purity and composition. Fig. 4(a) and Fig. 4(b) show the XRD patterns of NCO–CNF nanocomposite and CNF, respectively. Based on the XRD pattern of the hybrid nanocomposite (Fig. 4(a)), diffraction peaks observed at position $2\theta = 19.03^\circ$, 31.12° , 36.70° , 44.67° , 59.01° , and 64.77° correspond to (111), (220), (311), (400), (511), and (440) crystal planes, respectively, which can be well indexed to cubic NiCo_2O_4 with spinel structure (JCPDS card. No: 01-073-1702; Crystallographic parameters: Cubic $Fd3m$ (227); a, b , and

c (Å) = 8.1140; α, β , and γ ($^\circ$) = 90.00). Moreover, the XRD pattern of CNF (Fig. 4(b)) show broad diffraction peaks located at position $2\theta = 26.26^\circ$, 44.20° , and 50.59° which well correspond to (002), (101) and (102) crystal planes of hexagonal graphitic carbon (JCPDS card. No: 01-075-1621; Crystallographic parameters: Hexagonal $P6_3mc$ (186); a, b , and c (Å) = 2.4700, 2.4700, and 6.7900; α, β , and γ ($^\circ$) = 90.00, 90.00, and 120.00). The diffraction peaks corresponding to the graphitic carbon present on the hybrid NCO–CNF nanocomposite show significant shift to the left, such that from original position at $2\theta = 26.26^\circ$, 44.20° , and 50.59° , it can then be observed at 25.82° , 44.08° , and 50.22° ; this movement of the peaks is relevant as it may indicate the successful incorporation of NiCo_2O_4 to CNF structure [43].

X-ray photoelectron spectroscopy (XPS) was used to further investigate the chemical bonding state of the elements present on the synthesized hybrid NCO–CNF nanocomposite. Fig. 5(a) displays the full-survey spectrum of NCO–CNF nanocomposite, which confirm the presence of Ni 2p, Co 2p, O 1s and C 1s. Based on the spectrum of Ni 2p obtained using the Gaussian fitting method, shown in Fig. 5(b), the fitting peaks observed at 853.03 eV and 871.05 eV may corresponds to the Ni^{2+} ions located on the octahedral sites, while fitting peaks at 854.70 eV and 872.94 eV are Ni^{3+} ions located on the octahedral sites [44]. The remaining peaks at 860.25 eV and 878.49 eV are indexed as two shakeup satellites of Ni. Similarly, the spectrum of Co 2p (Fig. 5(c)) show the presence of two spin orbit doublets of Co^{2+} and Co^{3+} ions with two shakeup satellites of Co ions. Particularly, fitting peaks at 778.39 eV/793.36 eV and 779.87 eV/794.74 eV are indexed to Co^{3+} and Co^{2+} ions, occupying these octahedral and tetrahedral sites, respectively [45]. The obtained spectra of Ni 2p and Co 2p demonstrate the presence of both $\text{Ni}^{2+}/\text{Ni}^{3+}$ and $\text{Co}^{2+}/\text{Co}^{3+}$, which is parallel with the above chemical compositions of NCO–CNF nanocomposite discuss above. Fig. 5(d) show the spectrum of O 1s which illustrate four fitting peaks at 528.02 eV, 528.58 eV, 530.15 eV, and 531.76 eV denoted as O1, O2, O3, and O4, respectively. O1 and O2 may be attributed to the typical metal-oxygen bond and oxygen in hydroxyl groups, respectively, while O3 may be correlated to low oxygen coordination and small particle size that can be associated with the number of defects in the materials, and O4 is associated to

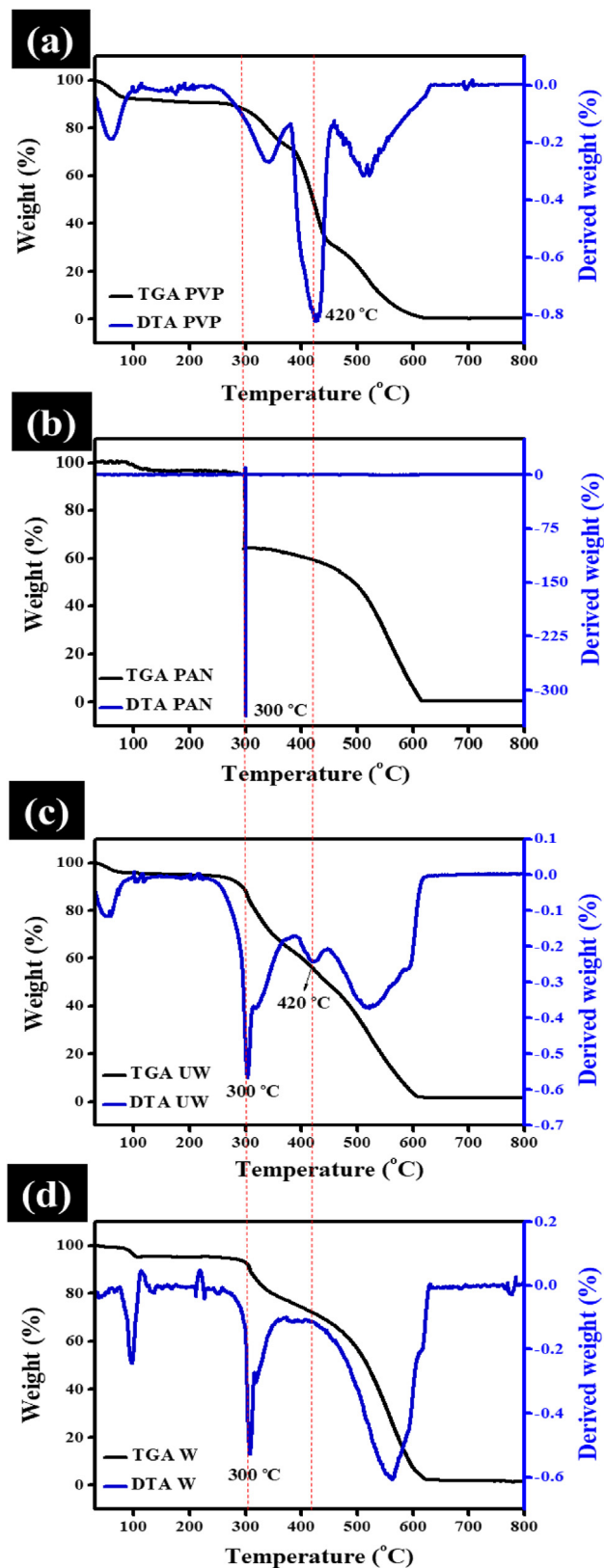


Fig. 1. TGA-DTA profiles of (a) PVP nf, (b) PAN nf, (c) PVP/PAN nf (fresh), and (d) PVP/PAN nf (washed).

the chemisorbed water molecules [46]. Lastly, the C 1s spectrum, shown in Fig. 5(e), confirmed the successful incorporation of NCO to the CNF, wherein fitting peaks at 282.77 eV, 283.48 eV, and 284.69 eV corresponds to sp^2 graphitic carbon, C–O, and C=O bonds, respectively [47].

Moreover, FESEM equipped with energy dispersive X-ray spectrometer was used to further analyse the structure and composition of the hybrid NCO–CNF nanocomposite. One important clarification, in here, only the fabricated CNF has the fibrous morphology even at its grinded form and nanometer size. Under high pressure and thermal controlled system during the hydrothermal treatment, the overall morphological structure of the material was formed. Fig. 6(a)–(d) show the low and high magnification FESEM images of the NCO–CNF nanocomposite, respectively. The final structure of the synthesized hybrid nanocomposite was a uniform dandelion-like morphology composing of cluster of numerous nanoneedle particles, which created an overall 3D structure morphology which is beneficial to enhance the physicochemical properties of the material. We suspect that the NiCo-precursor and hollow CNF, both in tenths of a nanometer size, were well incorporated to each other through chemisorption and that the hydrothermal condition had influenced or affected the final morphology formed. These assumptions were parallel with the XRD and XPS results, and were further supported by the high magnification HRTEM images together with the calculated d-spacing values and SAED ring pattern. Additionally, Fig. S2 shows the EDX elemental mapping which illustrate the uniform distribution of Ni, Co, O and C elements; this result further support our claim of successful formation of NCO–CNF nanocomposite.

As mentioned above, we further analysed the final morphology structure of the hybrid NCO–CNF nanocomposite by performing HRTEM analysis together with the calculation of d-spacing values and selected area electron diffraction (SAED). Fig. 7(a) and (b) show the HRTEM images of NCO–CNF nanocomposite at different magnification, wherein it focus on the detached nanoneedle particle from the dandelion-like nanoparticle. Based from the figure, the individual nanoneedle particle is composed of two distinct components which is represented by darker and lighter shade of nanoparticles. At higher magnification, we can assign the NCO to the darker nanoparticles while CNF represent the lighter nanoparticles. To support this assumptions, we measured the d-spacing values observed from HRTEM image. Based on Fig. 7(c), there are three (3) parts captured by HR-TEM, with 3 different direction of the parallel lines and 3 different shades, which may represent 3 different crystal planes. By averaging the distance between multiple points, we calculated the d-spacing values in each region and results are as follows: d-spacings = 2.889 Å, 2.456 Å, and 3.336 Å, which well correspond to (220), (311), and (002) crystal planes of spinel NCO and hexagonal graphitic carbon, respectively. Furthermore, we used the obtained diffraction rings from SAED observations to further support our assumptions. Fig. 7(d) shows the SAED ring patterns that are well indexed to (111), (002), (220), (311), (400), (511), and (440) crystal planes, which are parallel with the XRD pattern of the hybrid NCO–CNF nanocomposite. These results, strongly support the successful incorporation of spinel $NiCo_2O_4$ and hollow CNF through chemisorption during the hydrothermal treatment.

Finally, BET method and observed N_2 adsorption-desorption isotherm were used to determine the textural attributes of the hybrid nanocomposite such as surface area, pore volume, and average pore diameter. Fig. 7(e) display a typical type IV N_2 adsorption-desorption isotherm obtained by the sample with obvious hysteresis loop at relatively pressure range from 0.7 to 0.9. Additionally, inset figure shows the pore size sample mainly distributed between 0 and 50 nm size range. These results illustrate

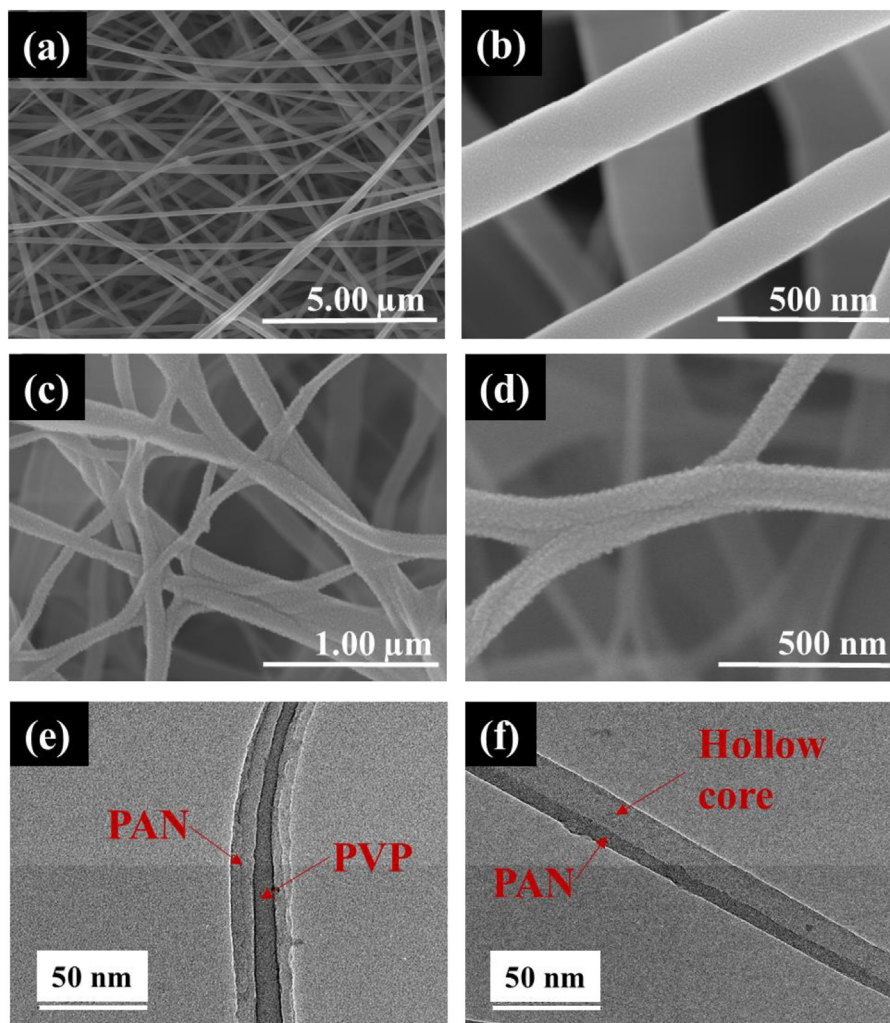


Fig. 2. (a) (c) Low and (b) (d) high magnification FESEM images of fresh and washed PVP/PAN nf, respectively. HR-TEM images of (c) fresh and (d) washed PVP/PAN nf.

the synthesized hybrid NCO–CNF nanocomposite is hierarchical mesoporous which consist of nanopores inside mesopores [48]; this type of pores is beneficial towards electrochemical activity as it will provide easier pathway for electron/electrolyte movement. Calculated surface area, pore volume and average pore size diameter based on BET method are $76.43 \text{ m}^2 \text{ g}^{-1}$, $0.2659 \text{ cm}^3 \text{ g}^{-1}$, and 6.06 nm , respectively.

3.3. Electrochemical measurements

All electrochemical measurements were performed in a three-electrode system using 2M KOH aqueous solution as electrolyte. To check the surface properties of our fabricated electrode towards the electrolyte, we conducted a contact angle measurement test using $5 \mu\text{L}$ of water. Based on Fig. S3 (cut images in the video), it can be easily tell that the surface of the electrode possessed a superhydrophilic surface wherein it has excess hydrophilicity or attraction towards water molecule. The water droplet penetrated through the electrode the moment it touched the surface. The Young's equation, however, cannot be used in this scenario as the system is fully dependent on the time; thus the contact angle may be resulted to 0° which is a characteristic of superhydrophilic surface. This characteristic of the surface of fabricated electrode is beneficial during the electron/electrolyte movement, as it can

effectively reduce the diffusion resistance between the electron, electrolyte and conductive substrate.

To check the electrochemical performance of the fabricated NCO–CNF @ NF substrate electrode, we initially stabilized the system by running 250 continuous cyclic voltammetry (CV) cycles at scan rate of 50 mV s^{-1} before proceeding to official measurements. Fig. 8(a) shows the CV curves obtained by the NCO–CNF @ NF electrode at increasing scan rates from 2 to 30 mV s^{-1} , with the corresponding anodic and cathodic peak current (A) vs square root of the scan rate (mV s^{-1})^{1/2} plot as inset. Based from the figure, the pair of redox peaks appeared between 0.1 and 0.55 V potential is a strong indication of the capacitance controlled by faradaic process, which involves rapid and reversible redox reactions between $\text{Ni}^{2+}/\text{Ni}^{3+}$ and $\text{Co}^{2+}/\text{Co}^{3+}$, and hydroxyl ions from the aqueous 2 M KOH electrolyte. Additionally, it can be observe that the redox peaks shifted to more anodic and cathodic directions with the increase in scan rate, which is mainly because of the development of overpotential that limits the faradaic reactions. In here, the plot of redox peak currents vs. square root of scan rates, shown in the inset of Fig. 8(a), shows a linear relationship which may confirm the surface controlled pseudocapacitive behaviour of the fabricated electrode. Additionally, using the relationship defined by Randles-Sevcik equation, the diffusion coefficient of the electroactive species can be determined. Accordingly, if the plot of the current peak against

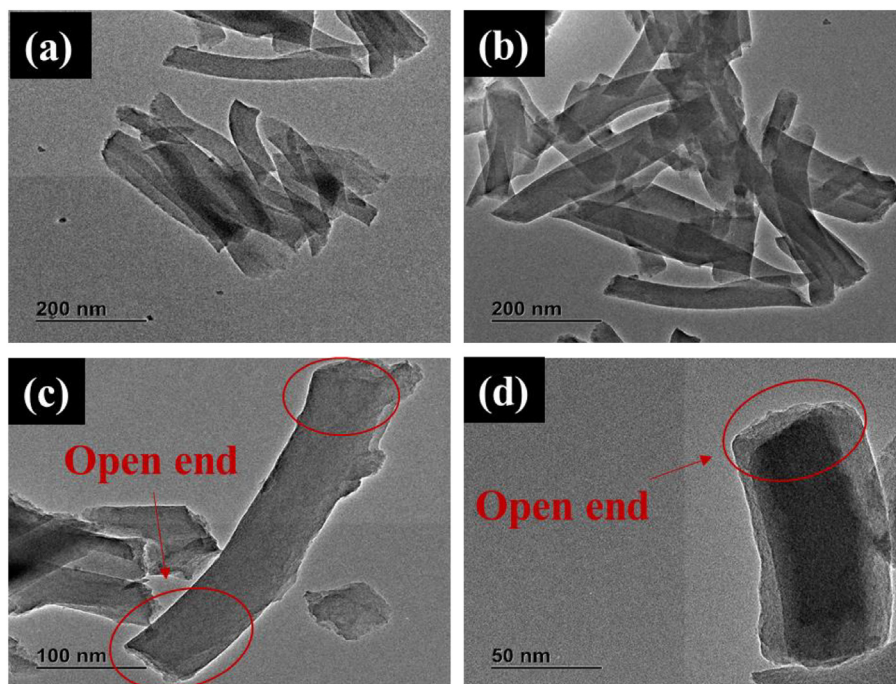


Fig. 3. (a) (b) Low and (c) (d) high magnification HRTEM images of the carbonized nanofiber.

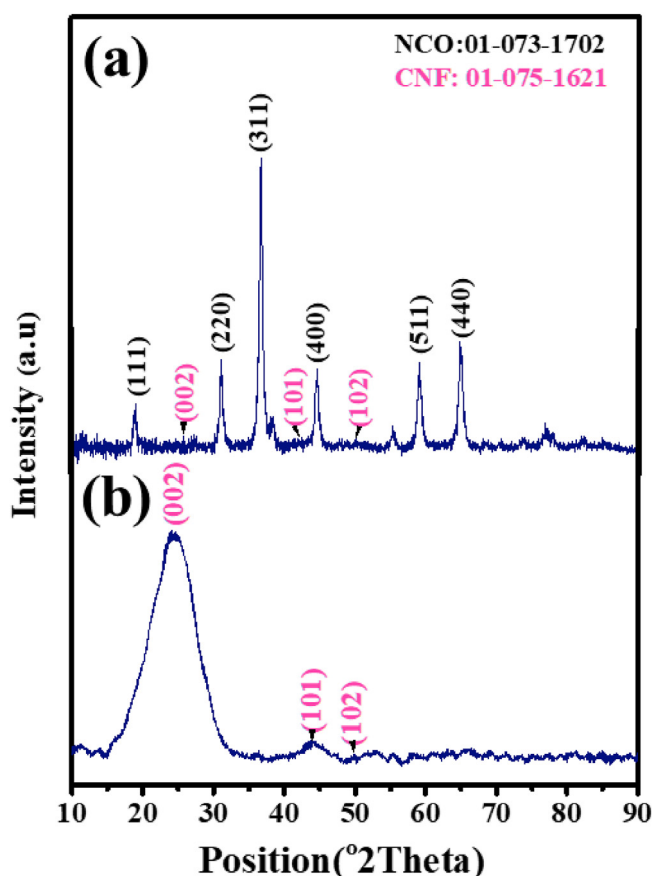
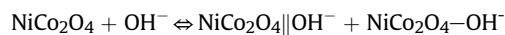


Fig. 4. XRD pattern of (a) NCO–CNF nanocomposite and (b) CNF.

the square root of the scan rate show a linear relationship, the diffusion coefficient can be obtained from the slope of the plot [49]. As shown in the inset, the plot of the anodic current peak against the square root of the scan rate show a linear relationship with diffusion coefficient equal to $19.18 \text{ cm}^2 \text{ s}^{-1}$.

More importantly, using the CV curve obtained at low scan rate of 2 mV s^{-1} , shown at Fig. 8(b), three distinct regions can be distinguished [50]; firstly, at -0.1 to 0.1 V , a rectangular shape without any redox peaks can be trace out from the CV curve (inset in Fig. 7(b)), which is a strong indication of electric double layer (EDL) capacitance behaviour; second, between 0.1 and 0.55 V , a clear pair of redox peaks appeared at 0.37 V and 0.22 V , respectively, which are ascribed to the faradaic redox reaction indicating a pseudocapacitance behaviour; and lastly, at 0.55 – 0.6 V , a sharp peak is obtained which corresponded to irreversible OER process – good indication that the NCO–CNF electrode has high electrocatalytic property.

Furthermore, the overall electrode/electrolyte mechanism can be expressed as the following [51]:



wherein the distinct rectangular curve at -0.1 to 0.1 V potential window represent the EDL formed between the electrode and the hydroxyl ions ($\text{NiCo}_2\text{O}_4\|\text{OH}^-$) [52], and the pair of redox peaks appeared at 0.1 – 0.55 V indicates the rapid and reversible redox reactions between $\text{Ni}^{2+}/\text{Ni}^{3+}$ and $\text{Co}^{2+}/\text{Co}^{3+}$, and hydroxyl ions ($\text{NiCo}_2\text{O}_4\text{--OH}^-$) from the aqueous 2 M KOH electrolyte [53]. Moreover, the presence of both EDL and faradaic redox reactions might be attributed to the graphitic CNF and spinel NiCo_2O_4 present in the electrode material, respectively; thus, the overall capacitance derived from the hybrid NCO–CNF electrode might be attributed from both electric double layer capacitance and pseudocapacitance. However, based on the integrated area of the rectangular curves and the faradaic redox reaction area, we can conclude that the specific capacitance is mainly dominated by the transition metal

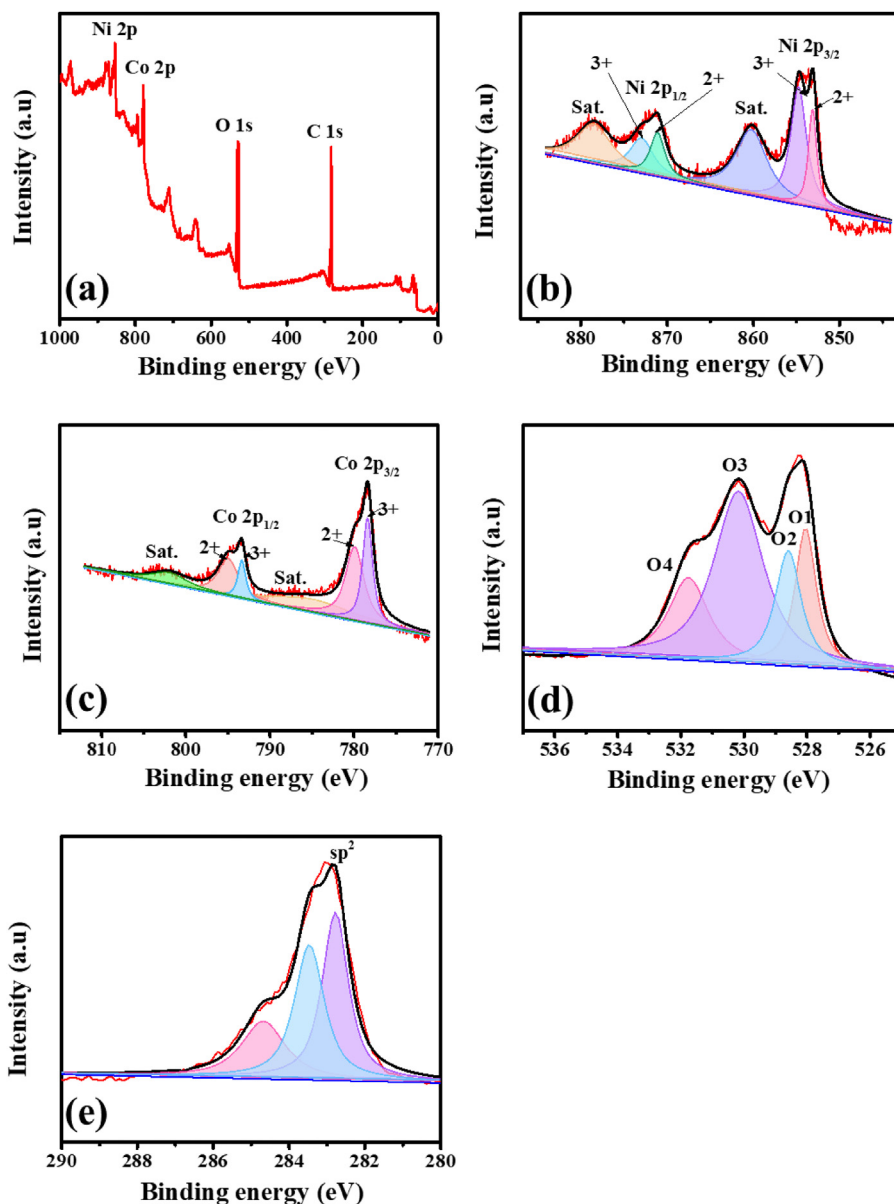


Fig. 5. (a) Full-survey spectrum of NCO–CNF nanocomposite, spectrum of (b) Ni 2p, (c) Co 2p, (d) O 1s, and (e) C 1s.

oxide part of the hybrid electrode. The specific capacitance calculated based on the integrated area of the CV curves at low scan rate of 2 mV s^{-1} resulted to a remarkably high specific capacitance equal to 3334.60 F g^{-1} . The decrease in the specific capacitance as the scan rate increase may indicate that the redox processes are diffusion limited; meaning that the inner active sites in the oxide layer are not readily accessible by the electrolyte at higher scan rates or current densities. The fast and reversible redox reaction is not complete with an increase in scan rate of the potential, leading to a decrease in the specific capacitance [54,55]. However, even though the specific capacitance gradually decreases upon the increase of scan rates, excellent specific capacitance of 990.28 F g^{-1} was still obtained even at 30 mV s^{-1} . Summary of the calculated specific capacitance based on the integrated area of CV curves at increasing scan rate are listed in Table 1.

To further evaluate the electrochemical performance of the hybrid NCO–CNF electrode, we performed a series of galvanostatic charge-discharge (GCD) tests using different current density from 5

to 50 A g^{-1} , and within $0.0\text{--}0.475 \text{ V}$ potential window. Parallel with the CV curves, the obtained GCD curves, shown in Fig. 8(c) and (d), can be divided into two distinct regions: (1) a sharp linear curve is visibly observed at $0.0\text{--}0.2 \text{ V}$ potential window, which is correlated with the electric double layer formed between the electrode/electrolyte interfaces [56], and (2) obvious voltage plateau is observed at $0.2\text{--}0.475 \text{ V}$ potential window, which indicates the faradaic redox reaction [57]. Similar with above observations, it can be concluded that though the overall capacitance is ascribed to both EDLC and pseudocapacitance, main capacitance is still attributed to the redox reaction between $\text{Ni}^{2+}/\text{Ni}^{3+}$ and $\text{Co}^{2+}/\text{Co}^{3+}$, and hydroxyl ions from the aqueous electrolyte. Furthermore, the calculated specific capacitance based on the discharge curve resulted to extraordinarily high value of 2991.96 F g^{-1} at 5 A g^{-1} current density. And even though the specific capacitance gradually decrease upon the increase of current density, still outstanding specific capacitance of 1188.19 F g^{-1} is obtained even at high current density of 50 A g^{-1} . Additionally, energy density was calculated based

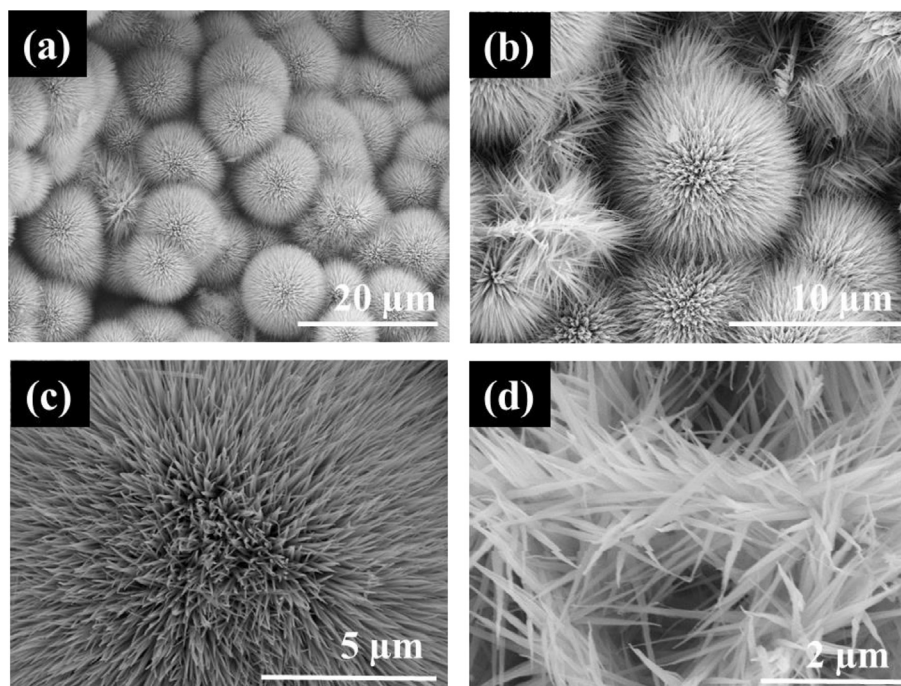


Fig. 6. FE-SEM images of NCO–CNF nanocomposite at (a)(b) low magnification and (c)(d) high magnification.

on the specific capacitance obtained from the discharge curve. One of the objective of every researcher working on supercapacitor is to increase the energy density of the system, and in this study we were able to obtained as high as $93.76 \text{ W h kg}^{-1}$ at 5 A g^{-1} current density, and was still able to retain a fair value of $37.23 \text{ W h kg}^{-1}$ even at high current density of 50 A g^{-1} . This is truly remarkable improvement on electrochemical performance of NiCo_2O_4 based electrode. Summary of the calculated specific capacitance and energy density based on the discharge curves at different current density are listed in Table 1.

Fig. 9(a) show the electrochemical impedance spectroscopy (EIS) measurement of the hybrid NCO–CNF electrode, with the inset images showing the transition point between high and low frequency, and the corresponding electric circuit diagram, respectively. Based on the Nyquist plot, the small diameter semicircle observed at the high frequency is correlated to the low charge transfer resistance (R_{ct}) value induced by the faradaic redox reaction and the electric double layer, respectively; thus imply the fast and easy charge transfer during the electrochemical process [58]. Additionally, the low value of equivalent series resistance (R_s) which is the combined ionic electrolyte resistance, electrode resistance, and interfacial resistance between electrode and conductive substrate, indicates high internal conductivity [59]. Furthermore, the inclined portion found in between the high and low frequency (mid frequency with angle $\sim 45^\circ$), is referred as Warburg resistance which is associated to the ion movement into the electrode/electrolyte interface [60]. Lastly, the vertical line observed at low frequency specifies a faster ion diffusion rate and typical supercapacitive behaviour [61]. Summary of the resistances value is listed in Table 2. Moreover, cycling stability test is very important property to evaluate since one of the main struggle of single NiCo_2O_4 up to this date is suffering from poor rate capability and inferior cycling stability because of its low electrical conductivity and small surface area. As we designed our hybrid NCO–CNF electrode, we aimed to achieve better cycling stability results at high current density. Fig. 9(b) shows the cycling stability of the

NCO–CNF using 3000 continuous GCD test at high current density of 30 A g^{-1} , and within $0.0\text{--}0.475 \text{ V}$ potential window. An outstanding capacity retention of 97.02% was achieved even after long cycles at high current density. The morphological structure of the material after the continuous cycling test at high current density of 30 A g^{-1} was examined via FESEM analysis. Based on the high magnification FESEM images of the material after cycling test, shown in Fig. S4, there are some structural changes that can be observed which can be attributed to the ions intercalation during the long and repeated cycling test. Formation of agglomerated particles in between of the nanoneedle particles (from the original dandelion like morphology), may be attributed to the OOH groups formed during the fast and reversible redox reactions between the $\text{Ni}^{2+/3+}/\text{Co}^{2+/3+}$ and hydroxyl ions from the electrolyte, thus making the final structure look expanded and exhausted. However, it is remarkable that even after long charge-discharge cycling test at high current density, the material still retained its original overall spherical shape which show great stability and was still capable to maintain majority of its original capacitance.

Lastly, we compare our obtained results to previous outstanding publish results for the last five years to further evaluate the electrochemical performance of our synthesized hybrid NCO–CNF electrode. For instance, Hao Tong et. Al [61] fabricated a binder-free NiCo_2O_4 @ 3D elastic N-doped hollow CNT sponge electrode, wherein they had obtained a fair result of specific capacitance and energy density 1074 F g^{-1} and $47.65 \text{ W h kg}^{-1}$ at 1 A g^{-1} current density, respectively. This result is lower compared to our hybrid NCO–CNF electrode which obtained a remarkably high specific capacitance and energy density of 2991.96 F g^{-1} and $93.76 \text{ W h kg}^{-1}$ at 5 A g^{-1} current density. Furthermore, two groups had done an almost similar study regarding a binder-free chemically deposited NiCo_2O_4 onto CNT film wherein both group obtained fair but lower results compared to our material; for instance, Shanshan Xu and group [43] fabricated NiCo_2O_4 chemically deposited on flexible CNT film obtained 828 F g^{-1} and $28.58 \text{ W h kg}^{-1}$ at 1 A g^{-1} current density, while Shihong Yue [47] fabricated almost same material

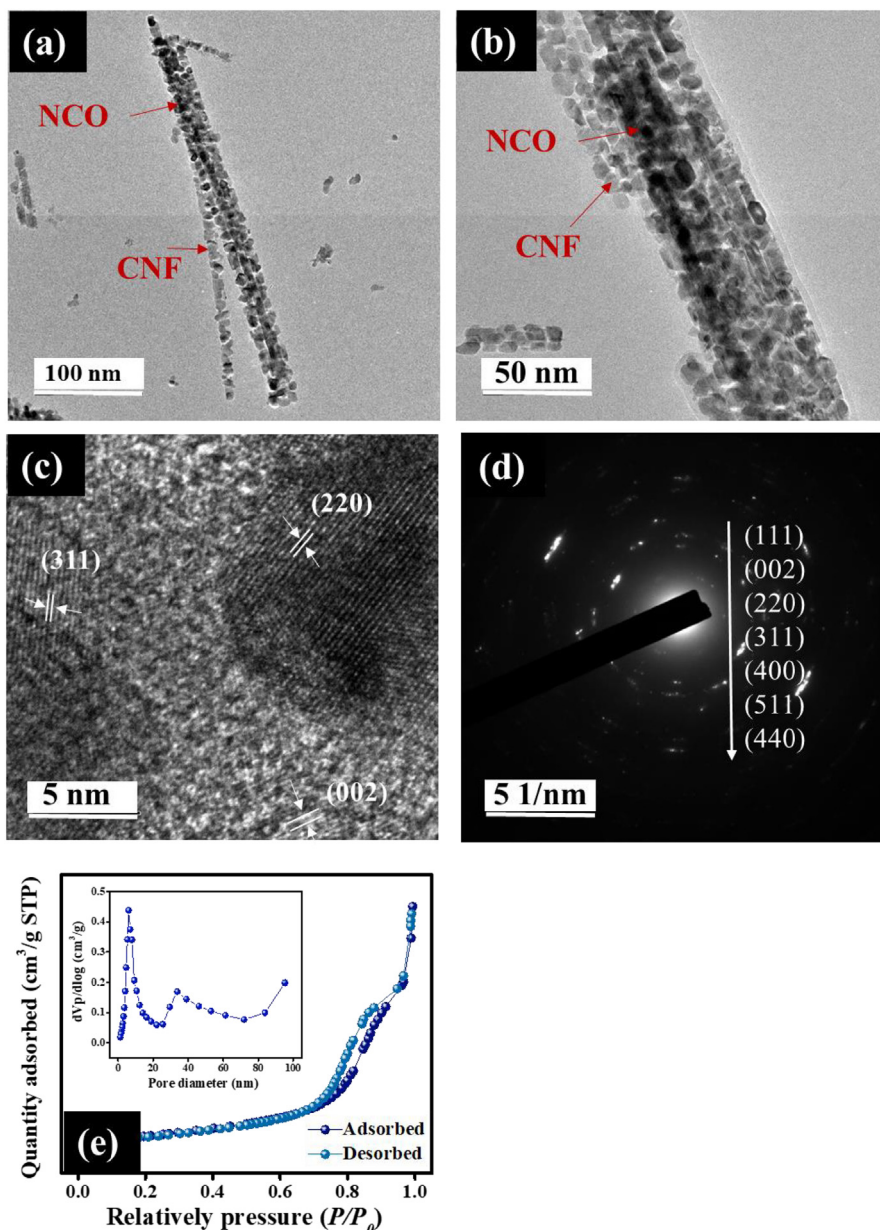


Fig. 7. (a) (b) HR-TEM image of NCO–CNF nanocomposite, (c) calculated d-spacing values, (d) SAED ring patterns, and (e) N_2 adsorption-desorption curve with BJH pore size distribution as inset.

but grown on graphene/CNT film and obtained 2292.2 F g^{-1} and $42.71 \text{ W h kg}^{-1}$ at 5 A g^{-1} current density, and using 6 M KOH aqueous electrolyte. These results are lower to ours even if we compare it with our highest current density (50 A g^{-1}) in which we have obtained specific capacitance and energy density as high as 1188.19 F g^{-1} and $37.23 \text{ W h kg}^{-1}$, respectively. Moreover, other groups such as Wei Xiong et al. [39] and Dongxuan Guo et al. [58], used biomass as source of their carbon material and incorporated it into NiCo_2O_4 . The method that they used may have lean into better environment, however the results that they have obtained are still lower compared to us. For instance, first group mentioned used mollusk shell as their macroporous carbon material obtained a reasonable result of specific capacitance and energy density of 1533 F g^{-1} and 48.3 W h kg^{-1} at 1 A g^{-1} current density, respectively; while second group who used dry honey pomelo peels as their biomass carbon source obtained 1137.5 F g^{-1} and $30.75 \text{ W h kg}^{-1}$ at 5 A g^{-1} current density.

These are great results considering their chosen raw materials, but compared to our electrospun hollow CNF, which is environmental friendly and cost efficient too, we can consider our results as more superior. Table 3 show the summary of our comparison wherein we listed down the significant parameters used during electrochemical measurements and the calculated specific capacitance and energy density based on the discharge curve.

As summary, we correlate the significant characterization analysis that we have done to the excellent electrochemical performance obtained by our hybrid NCO–CNF electrode. First on the list is the structural properties of the synthesized material which include (1) the hollow structure of fabricated CNF, (2) the dandelion-like final morphology of the hybrid NCO–CNF nanocomposite which composed of numerous nanoneedle particles consisting of CNF and NCO, and (3) the hierarchical mesoporous

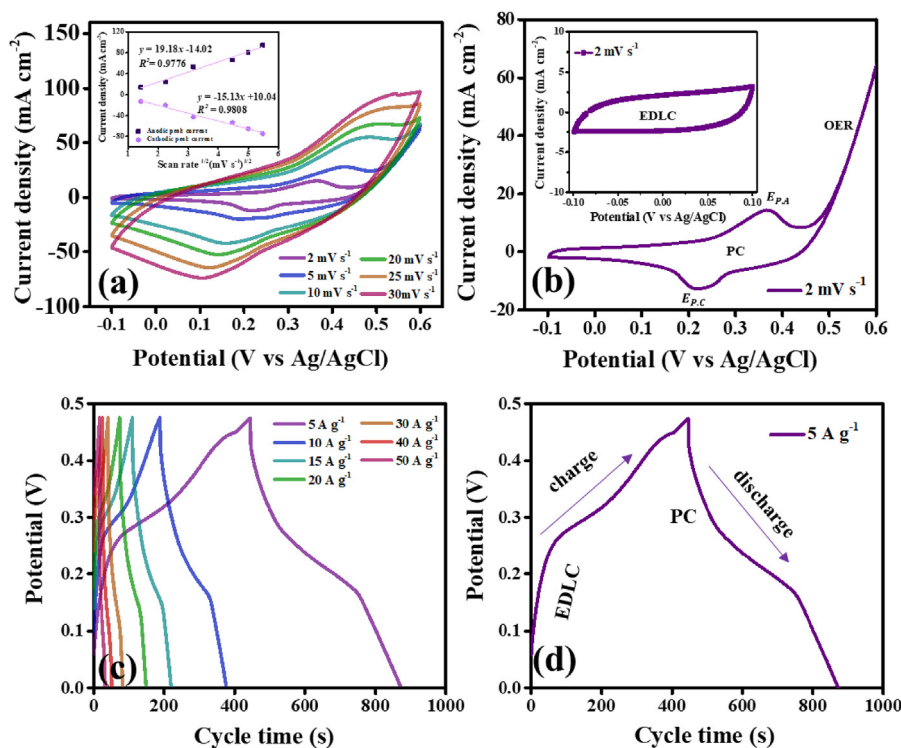


Fig. 8. CV curves at increasing scan rates from 2 to 30 mV s^{-1} , with the corresponding anodic and cathodic peak current (A) vs square root of the scan rate ($\text{mV s}^{-1})^{1/2}$ plot as insets, and (b) at 2 mV s^{-1} scan rate and inset showing the electric double layer obtained from -0.1 to 0.1 V potential window. GCD curve at (c) increasing current density from 5 to 50 A g^{-1} and (d) at 5 A g^{-1} current density.

Table 1

Summary of calculated electrochemical performance based on integrated area of CV curves and discharge curve from GCD.

Scan rate (mV s^{-1})	$C_{CV}(\text{F g}^{-1})$	Current density (A g^{-1})	$C_{GCD}(\text{F g}^{-1})$	ED (W. h kg^{-1})
2	3334.60	5	2991.96	93.76
5	2019.48	10	2646.84	82.94
10	1186.37	15	2302.08	72.14
20	1069.88	20	2085.14	65.34
25	1037.69	30	1746.11	54.72
30	990.28	40	1461.00	45.78
		50	1188.14	37.23

C_{CV} = specific capacitance based on integrated area of CV curve.

C_{GCD} = specific capacitance based on discharge curve of GCD.

ED = energy density.

surface and high surface area of the material. All of these structural properties are directly related to the provided shorten ion diffusion pathway and additional number of active sites which resulted to ultrafast electron/electrolyte movement during the electrochemical measurements. Second is the successful incorporation of NiCo_2O_4 and the hollow CNF, and the uniform growth of the NiCo -CNF precursors to the nickel foam substrate; both of which provided a conductive network that guaranteed the high speed movement of electron/electrolyte. Additionally, the fabrication of binder-free electrode thru direct growing of metal precursors onto the surface of substrate not only eliminated the use of any polymer binder that hinder some of the electro active sites, but also ensured the mechanical and chemical stability of the electrode. Lastly, EDLC and pseudocapacitance arising from both of the CNF and NCO, respectively, were added up together which effectively boost up the total specific capacitance of this hybrid electrode that lead to exceptional energy density and excellent cycling stability even at high current density.

4. Conclusions

In conclusion, we have successfully synthesized a hybrid nanocomposite based on synergistic mixture of hollow structure CNF and spinel NCO, with overall 3D nanostructure (with dandelion like morphology), hierarchical mesoporous surface, high specific surface area, and directly grown onto the surface of nickel foam substrate. According from the results of XRD and XPS analysis, the inclusive structure and composition of the designed hybrid material are well corresponded to the characteristics of both spinel NiCo_2O_4 and graphitic carbon; thus confirming the successful integration of NCO nanoparticles to the structure of hollow CNF. This was visually represented through the high resolution TEM images which demonstrated the synergistic mixture of the two components. The hollow structure of CNF provided a shorten ion diffusion pathway that served as highway to achieve an ultrafast electron/electrolyte movement and the numerous electroactive sites attributed to NCO structure enhanced the specific capacitance of the nanocomposite. Nevertheless, our results showed that the

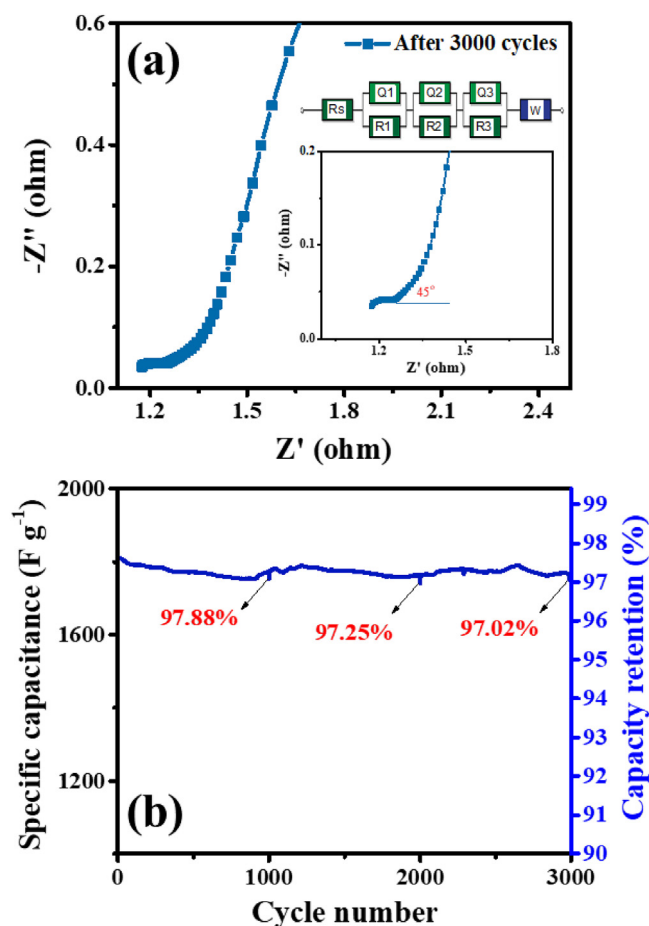


Fig. 9. (a) Nyquist plots with inset image showing the mid frequency point and the equivalent electric circuit diagram, and (b) cycling stability at high current density of $30 A g^{-1}$.

Table 2
Equivalent series resistance based on EIS analysis.

Condition	$R_s (\Omega)$	$R_1 (\Omega)$	$R_2 (\Omega)$	$R_3 (\Omega)$
After 3000 cycles	1.0297	2.5831	0.4139	0.2737

Table 3
Comparison list of the electrochemical performance of $NiCo_2O_4$ -C based electrode.

Electrode	Electrolyte	Current density ($A g^{-1}$)	C_{GCD} ($F g^{-1}$)	ED ($W h kg^{-1}$)	Reference
NCO @ CNT sponge	—	1	1074	47.65	[61]
NCO @ CNT film	2 M KOH	1	828	28.58	[43]
NCO @ graphene/CNT film	6 M KOH	5	2292	42.71	[47]
NCO-CNT @NF	1 M KOH	3	1533	48.30	[52]
NCO- mollusk carbon	2 M KOH	1	1696	8.47	[39]
NCO-biomass carbon	3 M KOH	5	1137	30.75	[58]
NCO-3D graphene	2 M KOH	1	2300	73.80	[53]
NCO-CNF @ NF	2 M KOH	5	2992	93.76	This work
		30	1746	54.72	This work
		50	1188	37.23	This work

NCO = $NiCo_2O_4$.

C_{GCD} = specific capacitance based on discharge curve of GCD.

ED = energy density.

derived capacitance of the NCO-CNF electrode is attributed to both pseudocapacitance and EDLC characteristics. We obtained outstanding results including remarkable specific capacitance and energy density values: $3339.60 F g^{-1}$ at low scan rate of $2 mV s^{-1}$, and $2991.96 F g^{-1}$ and $93.76 W h kg^{-1}$ at current density of $5 A g^{-1}$, respectively. Furthermore, the combined physical and electrochemical properties of fabricated binder-free hybrid NCO-CNF electrode, displayed superior electronic conductivity and efficient electron/electrolyte transfer that achieved specific capacitance and energy density as high as $1188.19 F g^{-1}$ and $37.23 W h kg^{-1}$, respectively, even at high current density of $50 A g^{-1}$. Lastly, the cycling stability of the NCO-CNF electrode is excellent as it retained 97.02% capacity retention even after 3000 continuous GCD cycles at high current density of $30 A g^{-1}$. Our fabricated NCO-CNF nanocomposite showed great potential as advanced electrode towards energy storage devices.

Acknowledgements

This work was supported by Basic Science Research Program through the National Research Foundation of Korea funded by the Ministry of Education (2018R1D1A1B07048146) and by the Korea Institute of Energy Technology Evaluation and Planning - Grants funded by the Ministry of Trade, Industry and Energy (No. 20174010201160).

Appendix A. Supplementary data

Supplementary data to this article can be found online at <https://doi.org/10.1016/j.electacta.2019.06.112>.

References

- [1] F. Wang, X. Wu, X. Yuan, Z. Liu, Y. Zhang, L. Fu, Chem. Soc. Rev. 46 (2017) 6816–6854.
- [2] G. Zhang, X. Xiao, B. Li, P. Gu, H. Xue, H. Pang, J. Mater. Chem. A 5 (2017) 8155–8186.
- [3] Y. Wang, Y. Song, Y. Xia, Chem. Soc. Rev. 45 (2016) 5925–5950.
- [4] D. Chen, Q. Wang, G. Shen, J. Mater. Chem. A 3 (2015) 10158–10173.
- [5] K. Ho, L. Li, J. Mater. Chem. A 7 (2019) 3516–3530.
- [6] W. Liu, K. Wang, C. Li, X. Zhang, X. Sun, J. Han, X. Wu, Y. Ma, J. Mater. Chem. A 8 (2018) 18–22.
- [7] Q. Wang, J. Yan, Z. Fan, Energy Environ. Sci. 9 (2016) 729–762.
- [8] J. Kim, J. Lee, J. You, M. Park, S. Al Hossain, J. Ho, Mater. Horizons. 3 (2016) 517–535.
- [9] M. Park, J. Kim, J. Kim, J. Lee, H. Kim, Phys. Chem. Chem. Phys. 17 (2015) 30963–30977.
- [10] X. Mu, J. Du, Y. Zhang, Z. Liang, H. Wang, B. Huang, J. Zhou, X. Pan, Z. Zhang, E. Xie, ACS Appl. Mater. 9 (2017) 35775–35784.
- [11] Y. Zheng, Z. Lin, W. Chen, B. Liang, H. Du, R. Yang, X. He, Z. Tang, X. Gui, J. Mater. Chem. A 5 (2017) 5886–5894.
- [12] Z. Zhang, K. Chi, F. Xiao, S. Wang, J. Mater. Chem. A 3 (2015) 12828–12835.
- [13] Y. Zhou, N. Lachman, H. Xu, D. Bhattacharya, P. Fattahi, M.R. Abidian, S. Wu, K.K. Gleason, B.L. Wardle, Q.M. Zhang, J. Mater. Chem. A 2 (2014) 9964–9969.
- [14] Y. Li, X. Han, T. Yi, Y. He, X. Li, J. Energy Chem. 31 (2019) 54–78.
- [15] J. Zhao, C. Li, Q. Zhang, J. Zhang, X. Wang, Z. Lin, J. Wang, W. Lv, C. Lu, C. Wong, Y. Yao, J. Mater. Chem. A 5 (2017) 6928–6936.
- [16] X. Zheng, Y.Y., Q. Yang, B. Geng, X. Zhang, Dalton Trans. 45 (2016) 572–578.
- [17] Y. Wang, C. Shen, L. Niu, R. Li, H. Guo, J. Mater. Chem. A 4 (2016) 9977–9985.
- [18] A. Borenstein, O. Hanna, R. Attias, S. Luski, J. Mater. Chem. A 5 (2017) 12653–12672.
- [19] H. Wang, L. Hu, C. Wang, Q. Sun, H. Li, T. Zhai, J. Mater. Chem. A 7 (2019) 3632–3641.
- [20] Y. Yan, J. Miao, Z. Yang, F. Xiao, H.B. Yang, B. Lui, Y. Yang, Chem. Soc. Rev. 44 (2015) 3295–3346.
- [21] H. Xue, X. Mu, J. Tang, X. Fan, H. Gong, T. Wang, J. He, Y. Yamauchi, J. Mater. Chem. A 4 (2016) 9106–9112, <https://doi.org/10.1039/c6ta01712f>.
- [22] W. Li, M. Li, K.R. Adair, X. Sun, Y. Yu, lithium-ion and sodium-ion batteries, J. Mater. Chem. A 5 (2017) 13882–13906.
- [23] Y. Zhao, J. Zhang, K. Li, Z. Ao, C. Wang, H. Liu, K. Sun, G. Wang, J. Mater. Chem. A 4 (2016) 12818–12824.
- [24] D. Yigit, F. Soysal, T. Gungor, B. Cicek, M. Gullu, RSC Adv. 7 (2017) 41419–41428.
- [25] J.W. Sung, C.L. Lee, S. Yu, I.D. Kim, J. Mater. Chem. A 4 (2016) 703–750.
- [26] B.J. Lee, K.M. Park, W.R. Yu, J.H. Youk, Macromolecules Research 20 (2012)

- 605–613.
- [27] R. Khajavi, M. Abbasipour, *Sci. Iran. F* 19 (2012) 2029–2034.
- [28] J.S. Huang, T. You, *Advances in Nanofibers*, Russel Maguire IntechOpen, 2013, <https://doi.org/10.5772/57099>.
- [29] D.S. Sun, Y.H. Li, Z.Y. Wang, X.P. Cheng, S. Jaffer, Y.F. Zhang, *J. Mater. Chem. A* 4 (2016) 5198–5204.
- [30] D.M. Alqahtani, C. Zequine, C.K. Ranaweera, K. Siam, P.K. Kahol, T. Prasad, S.R. Mishra, R.K. Gupta, *J. Alloy. Comp.* 771 (2019) 951–959.
- [31] D.A. Agyeman, M. Park, Y. Kang, *J. Mater. Chem. A* 5 (2017) 22234–22241.
- [32] S. Kwun, N. Hui, C. Ouyang, S. Chan, *J. Mater. Chem. A* 6 (2018) 10647–10685.
- [33] G.M. Tomboc, H.S. Jadhav, H. Kim, *Chem. Eng. J.* 308 (2017) 202–213.
- [34] Y. Xiao, J. Huang, Y. Xu, H. Zhu, K. Yuan, Y. Chen, *J. Mater. Chem. A* 6 (2018) 9161–9171.
- [35] M. Guo, J. Balamurugan, T.D. Thanh, N.H. Kim, J.H. Lee, *J. Mater. Chem. A* 4 (2016) 17560–17571.
- [36] N. Hameed, J. Sharp, S. Nunna, C. Creighton, K. Magniez, P. Jyotishkumar, N.V. Salim, B. Fox, *Polym. Degrad. Stabil.* 128 (2016) 39–45.
- [37] K.M. Koczkur, S. Mourdikoudis, L. Polavarapu, S.E. Skrabalak, *Dalton Trans.* 44 (2015) 17883–17905.
- [38] F.O. Agyemang, G.M. Tomboc, S. Kwofie, H. Kim, *Electrochim. Acta* 259 (2018) 1110–1119.
- [39] W. Xiong, Y. Gao, X. Wu, X. Hu, D. Lan, Y. Chen, X. Pu, Y. Zeng, J. Su, Z. Zhu, *ACS Appl. Mater.* 6 (2014) 19416–19423.
- [40] Y. Zhu, Z. Wu, M. Jing, H. Hou, Y. Yang, Y. Zhang, *J. Mater. Chem. A* 3 (2014) 866–877.
- [41] J. Balamurugan, T.D. Thanh, N.H. Kim, J.H. Lee, *J. Mater. Chem. A* 4 (2016) 9555–9565.
- [42] R.F. Ribeiro, L.C. Pardini, N.P. Alves, C. Alberto, R. Brito, *Pollmeros* 25 (2015) 523–530.
- [43] S. Xu, D. Yang, F. Zhang, J. Liu, *RSC Adv.* 5 (2015) 74032–74039.
- [44] C. Yu, Y. Wang, J. Zhang, X. Shu, J. Cui, Y. Qin, H. Zheng, J. Liu, Y. Zhang, Y. Wu, *New J. Chem.* 40 (2016) 6881–6889.
- [45] G.M. Tomboc, F.O. Agyemang, H. Kim, *Electrochim. Acta* 263 (2018) 362–372.
- [46] A. Ganguly, S. Sharma, P. Papakonstantinou, J. Hamilton, *J. Phys. Chem. C* 115 (2011) 17009–17019.
- [47] S. Yue, H. Tong, L. Lu, W. Tang, W. Bai, F. Jin, Q. Han, J. He, J. Liu, X. Zhang, *J. Mater. Chem. A* 5 (2017) 689–698.
- [48] G.M. Tomboc, M.W. Abebe, A.F. Baye, H. Kim, *J. Energy Chem.* 29 (2019) 136–146.
- [49] A. Sarkar, A. Singh, D. Sarkar, G.G. Khan, K. Mandal, *ACS Sustain. Chem. Eng.* 3 (2015) 2254–2263.
- [50] R. Ding, L. Qi, M. Jia, H. Wang, *Electrochim. Acta* 107 (2013) 494–502.
- [51] R.R. Salunkhe, K. Jang, H. Yu, S. Yu, T. Ganesh, S. Han, H. Ahn, *J. Alloy. Comp.* 509 (2011) 6677–6682.
- [52] X. Li, W. Sun, L. Wang, Y. Qi, T. Guo, *RSC Adv.* 5 (2015) 7976–7985.
- [53] S. Sun, S. Wang, S. Li, Y. Li, Y. Zhang, J. Chen, Z. Zhang, S. Fang, P. Wang, *J. Mater. Chem. A* 4 (2016) 18646–18653.
- [54] S. Maiti, A. Pramanik, S. Mahanty, *CrystEngComm* 18 (2016) 450–461.
- [55] J. Wen, S. Sun, B. Zhang, N. Shi, X. Liao, G. Yin, Z. Huang, X. Pu, *RSC Adv.* 9 (2019) 4693–4699.
- [56] D.H. Nagaraju, Q. Wang, P. Beaujuge, H.N. Alshareef, *J. Mater. Chem. A* 2 (2014) 17146–17152.
- [57] C. Dong, Y. Wang, J. Xu, G. Cheng, W. Yang, T. Kou, Z. Zhang, Y. Ding, *J. Mater. Chem. A* 2 (2014) 18229–18235.
- [58] D. Guo, L. Zhang, X. Song, L. Tan, *New J. Chem.* 42 (2018) 8478–8484.
- [59] H. Cnt, O. Nico, F. Cai, Y. Kang, H. Chen, Q. Li, *J. Mater. Chem. A* 2 (2014) 11509–11515.
- [60] L. Chen, J. Zhu, *Chem. Commun.* 50 (2014) 8253–8256.
- [61] H. Tong, S. Yue, L. Lu, F. Jin, Q. Han, X. Zhang, J. Liu, *Nanoscale* 9 (2017) 16826–16835.